ELSEVIER

International Journal of Heat and Fluid Flow 23 (2002) 807–822

International Journal of HEAT AND FLUID FLOW

www.elsevier.com/locate/ijhff

A model for droplet entrainment in heated annular flow

M.J. Holowach *, L.E. Hochreiter, F.B. Cheung

Department of Mechanical and Nuclear Engineering, The Pennsylvania State University, 137 Reber Building, University Park, PA 16802-1412, USA

Received 1 April 2002; accepted 20 June 2002

Abstract

The ability to accurately predict droplet entrainment in annular two-phase flow is required to effectively calculate the interfacial mass, momentum, and energy transfer, which characterizes nuclear reactor safety, system design, analysis, and performance. Most annular flow entrainment models in the open literature are formulated in terms of dimensionless groups, which do not directly account for interfacial instabilities. However, many researchers agree that there is a clear presence of interfacial instability phenomena having a direct impact on droplet entrainment. The present study proposes a model for droplet entrainment, based on the underlying physics of droplet entrainment from upward co-current annular film flow that is characteristic to light water reactor safety analysis. The model is developed based on a force balance and stability analysis that can be implemented into a transient three-field (continuous liquid, droplet, and vapor) two-phase heat transfer and fluid flow systems analysis computer code.

Keywords: Droplet entrainment; Annular film flow; Safety analysis

1. Introduction

An understanding of the physical phenomena leading to the entrainment of liquid droplets by a gas flow is of considerable practical importance for the effective modeling of heat and mass transfer processes in two-phase systems (Ishii and Grolmes, 1975). The mechanisms of interfacial mass, momentum, and energy transfer between phases are significantly altered by the entrainment of liquid. The entrainment of liquid can occur under reactor safety analysis considerations due to two distinctly different situations in upward co-current two-phase vertical flow. Droplet entrainment can result from situations in which a gas is flowing over a liquid film such as in annular film flow. A schematic representation of the entrained liquid flow from annular film flow is given in Fig. 1. A second means for droplet entrainment occurs at a quench front or within a froth region when vapor bubbles up through a pool, and/or vapor is being generated due to the quenching phenomenon. The present study focuses on the first situation examined which is the droplet entrainment from an annular film.

The ability to predict droplet entrainment in these distinct situations is required to calculate the mass, momentum, and energy transfer in two-phase flow under transient conditions for reactor safety analysis. For example, the critical heat flux (CHF) and post-critical heat flux (post-CHF) in light-water cooled reactors as well as the effectiveness of emergency core cooling systems in water reactors are all significantly affected by the entrainment of liquid droplets in the vapor core flow (Ishii and Grolmes, 1975).

In the case of a transient thermal hydraulic systems analysis computer code utilized for nuclear reactor safety calculations, there is a need to accurately calculate droplet entrainment for the geometrical configuration that is modeled with a thermal hydraulic node scheme. Additionally, since many two-phase flow processes are time-varying in nature, there is a necessity to develop a droplet entrainment model that is based on fundamental physics and has the requisite flexibility to be used in transient system calculations.

In modeling droplet entrainment in annular film flow, many of the macroscopic-parameter based models

* Corresponding author. Tel.: +1-814-865-2289; fax: +1-814-865-8499.

E-mail address: mjholowach@psu.edu (M.J. Holowach).

0142-727X/02/$ - see front matter © 2002 Elsevier Science Inc. All rights reserved.
PII: S0142-727X(02)00194-7

Nomenclature

a	amplitude of the sine wave
$\tilde{a}$	height of the wave crest that is sheared off
b	the distance from the y-axis to the point of the sine wave at height $a-\tilde{a}$
A_{cv}	the interfacial area in the control volume
$A_{entr,w}$	frontal area of wave crest
A_σ	area on which the surface tension force acts
c	wave velocity
C_D	drag coefficient
C_w	dimensionless parameter (Ishii and Grolmes, 1975)
D_H	hydraulic diameter
f_{il}	interfacial friction factor based on liquid flow rate
f_{ig}	interfacial film friction factor based on gas flow rate
g	gravitational acceleration
G_g	vapor mass flux
G_e	entrained mass flux
k	wave number
K	curvature
m	film thickness
$N_{w,cv}$	number of waves in the control volume
N_{il}	normal stress exerted by the liquid phase on the interface
N_{iG}	normal stress exerted by the gas core phase on the interface
N_μ	viscosity number
P	pressure
Re_f	Reynolds number (based on liquid film flow rate),
Re_g	Reynolds number (based on vapor flow rate)
Re_{gc}	Reynolds number (based on gas core mixture flow rate)
S_E	droplet entrainment flux (mass flow rate per unit interfacial area, kg/m^{2}s)
$\bar{u}_G$	mean gas velocity
$\bar{u}_{gc}$	average velocity of the gas core
$\bar{u}_L$	mean film velocity
$V_{entr,w}$	the volume of liquid entrained from a wave crest
P_w	wetted perimeter
$V_{gc,sup}$	superficial gas core mixture velocity
v_f	film velocity
w_g	vapor mass flow rate
w_e	entrained droplet mass flow rate

Greeks

α_l	volume fraction occupied by continuous liquid
α_e	volume fraction occupied by entrained liquid
α_v	void fraction
λ	wavelength
μ	dynamic viscosity
ν	kinematic viscosity
ρ	density
σ	surface tension
$\tau_{w,cv}$	period of the entrainment phenomena in the control volume
τ_i	interfacial shear stress
χ	curvature

Subscripts

bl	boundary layer
c	critical (wavelength)
f	fluid
g	vapor
gc	gas core mixture

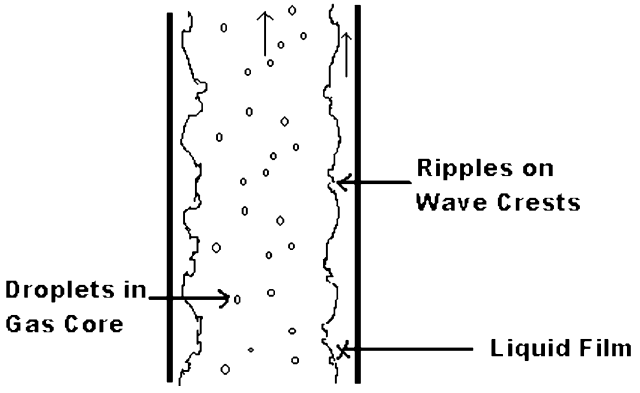

Fig. 1. Schematic representation of co-current annular two-phase flow.

currently available in the open literature are not developed to predict the droplet entrainment rate, but rather an equilibrium entrained droplet fraction. As a result, these models are of limited use in a computer code calculation that is performed to model transient and/or developing fluid flow and heat transfer.

This work presents the development and evaluation of a physical model for droplet entrainment in an upward co-current annular two-phase flow. The model that is proposed has the physical representation of the entrainment phenomena as is currently understood. The methodology for modeling droplet entrainment in annular two-phase flow that is proposed can also serve as the basis for the future development of a more physi-

cally based entrainment model characterizing the quench front/froth region during the reflood phase of a postulated nuclear reactor accident.

2. Current approach in entrainment modeling

Most annular flow entrainment models in the open literature are strongly dependent on dimensionless groups, and have a limited dependency on the physical processes of entrainment. Many researchers agree that there is a clear presence of interfacial instability phenomena affecting annular entrainment, though most available models do not directly account for this effect (Lopez de Bertodano et al., 2001; Miesen, 1994). Due to the complex nature of the annular entrainment phenomenon, it has been more convenient and computationally efficient to model the droplet entrainment rate utilizing dimensionless groups such as the Reynolds number and Weber number rather than a physically based model. Reasonable results have been obtained over a limited range of conditions and fluids using such methods, but there is limited applicability over a wide range of conditions due to the empirical nature of the available models. Also, many of the current annular flow entrainment models simply calculate the equilibrium entrainment within the flow, which is of limited use in a transient two-phase flow computer code since the flow many not be in mechanical and/or thermal equilibrium. Many of the available entrainment models, such as the model currently employed in COBRA-TF (Thurgood et al., 1983), utilize an interfacial drag term that is calculated based on steady-state air–water data. Though this model can reasonably predict the droplet entrainment rate over a limited range of conditions, it can also predict the entrainment for the wrong reason in a steam–water nuclear reactor environment. The use of an air–water interfacial drag model can significantly over-predict the drag in a steam–water environment as indicated by Hossfeld et al. (1982).

3. Development of an upward co-current annular flow droplet entrainment model

Using high-speed cinematography, Woodmansee and Hanratty (1969) observed that the primary means of droplet entrainment from a liquid film occurs by the rapid acceleration, lifting, and subsequent shattering of ripples present in the liquid roll wave structure. The lifetime of these ripples was observed to be short compared to that of the roll wave, indicating that many such ripples cause the droplet entrainment through the life of the roll wave, meaning that the roll wave structure has less effect on entrainment than the rapid lifting and shattering of the ripples present on the roll wave. From

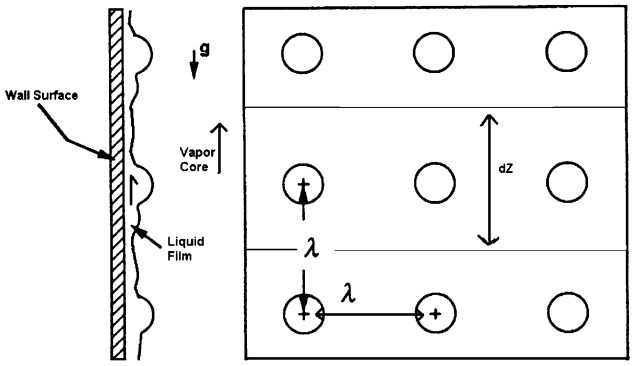

Fig. 2. Entrainment control volume and postulated pattern of wavelet distribution.

these visual observations, Woodmansee and Hanratty (1969) postulated that droplet entrainment in annular film flow primarily results from a Kelvin–Helmholtz instability where the destabilizing force is the pressure variation caused by the compression of the gas streamlines at the crests of the wavelets. Therefore, in the development of a physical model for droplet entrainment in annular two-phase flow, the Kelvin–Helmholtz instability should be used as an underlying basis.

By performing a control volume analysis on a particular axial height, dz, of a region which represents the distribution of ripples contributing to entrainment (sketched in Fig. 2), a general expression can be formed for the droplet entrainment rate. The droplet entrainment rate is a function of the volume of liquid swept off of each wave, the wavelength, the number of waves in the control volume, and the velocity at which the waves travel through the control volume. This general expression is given as:

$$S_{\mathrm{E}} = \frac{V_{\mathrm{entr,w}} \rho_{\mathrm{f}} N_{\mathrm{w,cv}}}{A_{\mathrm{cv}} \tau_{\mathrm{w,cv}}} \tag{1}$$

For the relationship given above, S_{E} is the droplet entrainment flux (entrainment rate per unit interfacial area, kg/m^{2}s), $V_{\mathrm{entr,w}}$ the volume of liquid entrained from a wave crest, ρ_{f} is the liquid density, $N_{\mathrm{w,cv}}$ the number of waves in the control volume, A_{cv} the interfacial area in the control volume, and $\tau_{\mathrm{w,cv}}$ the period of the entrainment phenomena in the control volume.

Using Eq. (1) as the basis for entrainment rate within a control volume, the following discussions develop the derivations and assumptions for the specific terms given in Eq. (1).

Since the underlying physical behavior for the droplet entrainment phenomenon in annular film flow is believed to be the Kelvin–Helmholtz instability as observed by Woodmansee and Hanratty (1969), a discussion and derivation of the criterion for interfacial stability is appropriate at this point. The scenario of interfacial stability for vertical upward co-current flow

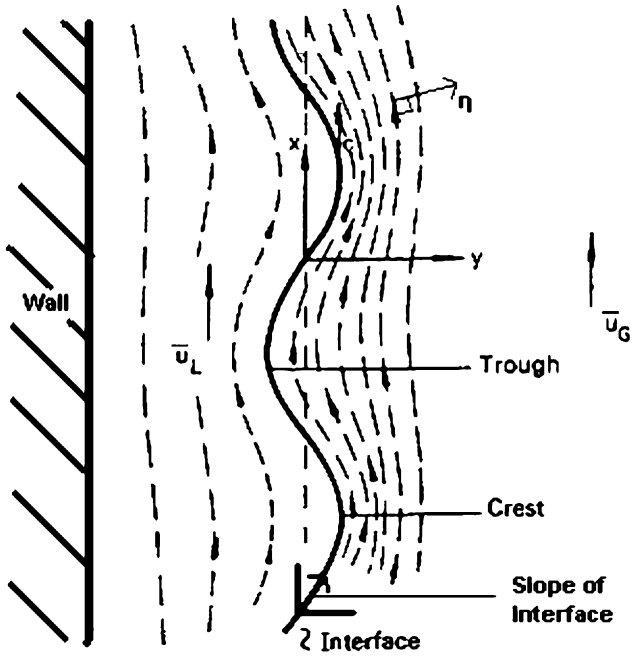

Fig. 3. Streamlines in two-phase flow with a wavy interface (Hewitt and Hall-Taylor, 1970).

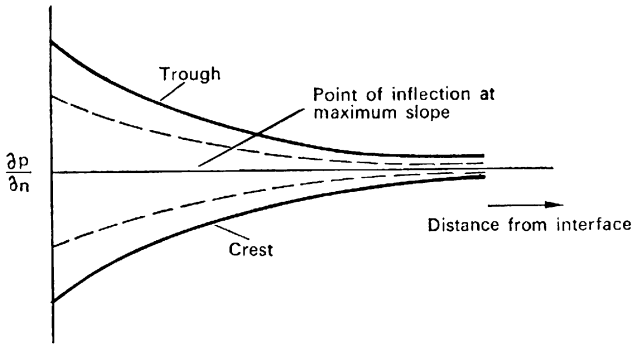

Fig. 4. Pressure gradient normal to a wavy interface (Hewitt and Hall-Taylor, 1970).

of a gas and liquid phase is discussed in detail by Hewitt and Hall-Taylor (1970) and Holowach (2002).

Consider the case in which the flow of two inviscid fluids of different densities (such as a gas and a liquid) separated by a vertical interface on which waves of wavelength, λ, are moving with a velocity, c. This scenario, which is quite similar to that of vertical annular two-phase flow is schematically detailed in Fig. 3. Hewitt and Hall-Taylor (1970) approached this scenario by simplifying the problem by considering the action of the two phases separately with the forces exerted by the gas phase on the wavy boundary being first evaluated and then the subsequent effects on the liquid phase being assessed.

Fig. 3 displays the streamlines of the flow for a mean gas velocity of $\bar{u}_G$ and a mean film velocity of $\bar{u}_L$. In viewing Fig. 3, one should note that the amount of distortion of the streamlines decreases as distance from the interface increases. Hewitt and Hall-Taylor (1970) explained that as the gas flows around the liquid wave, centrifugal forces are set up, and these must be balanced by a pressure gradient in the direction normal to the streamline as seen in Fig. 4.

3.1. Interfacial stability calculation

In this calculation, an expression is arrived to determine the critical wavelength at which the interface becomes unstable for a given set of fluid conditions. In order to arrive at this critical wavelength, the stability of the interface between the gas and the liquid is analyzed on the basis of a small perturbation assuming that the interface slope (represented in Fig. 3) is small. Subsequently, the equations of fluid motion can be linearized so as to provide a simplified solution that can be applied to the analysis of the entrainment phenomenon. The calculation presented by Hewitt and Hall-Taylor (1970) is used as a basis for this analysis, but has been modified to account for a homogeneous gas and droplet mixture in the gas core, and to additionally account for film thickness effects in more detail. The rigorous development of the stability analysis is presented in the dissertation of Holowach (2002), with the end results discussed in this work.

Considering the waves generated in annular two-phase flow that cause droplet entrainment, for positive values of the imaginary component of the wave velocity, the wave amplitude will increase exponentially with time. For negative values of the imaginary component of the wave velocity, the wave amplitude will decrease exponentially with time. When the imaginary component of the wave velocity is equal to zero, the wave amplitude will remain constant.

Therefore, the problem of interfacial stability, which is associated with droplet entrainment, can be related to the specific fluid flow parameters that cause the imaginary component of the wave velocity to be greater than zero. The determination of the parameters which characterize the limiting stable wave will allow for the development of a physical entrainment model based on a limiting set of geometric conditions.

In this analysis, the flow is considered to be axisymmetric, and the behavior of the gas and liquid phases is analyzed separately. The gas phase is considered to consist of both entrained droplets and vapor moving in the "core" of the annular flow.

Additionally, in this stability analysis, the derivations assume inviscid core and film flow. Though most of the annular film entrainment scenarios of concern in reactor safety analysis can exhibit both turbulent film and/or vapor core flow, the inviscid solution of the stability problem is presented in this section to provide a basis for the understanding of the instability phenomenon

and estimation of an appropriate length scale for the wavelets which contribute to the droplet entrainment. With this basis, an extension can be made to apply this stability analysis to conditions of turbulent core and film flow based on the success of similar stability analyses in their application and modeling of turbulent two-phase flow related phenomena such as the classical Zuber pool boiling model which is based on a similar hydrodynamic instability (Zuber et al., 1961).

3.1.1. Gas core analysis

The density and the velocity of the gas core must be defined for the purposes of this analysis. Parameters used to calculate the gas core properties have been selected that are readily available, and calculated in two-phase fluid flow and heat transfer computer codes such as densities, flow rates, and volume fractions. The gas core density and average velocity are arrived at using a homogeneous flow assumption.

The density of the gas core, ρ_{gc}, is defined in terms of the void fraction, α_v, and the volume fraction occupied by entrained liquid, α_e:

$$\rho_{gc} = \rho_g \frac{\alpha_v}{\alpha_e + \alpha_v} + \rho_f \frac{\alpha_e}{\alpha_e + \alpha_v} \tag{2}$$

The average velocity of the gas core, $\bar{u}_{gc}$, is defined in terms of the vapor and entrained liquid flow rates (w_g and w_e, respectively), the gas core density, the void fraction, volume fraction occupied by entrained liquid, and the channel diameter:

$$\bar{u}_{gc} = \frac{w_g + w_e}{\pi \frac{d^2}{4} (\alpha_e + \alpha_v) \rho_{gc}} \tag{3}$$

Utilizing the assumed properties of the gas core, the analysis of the gas core follows the conventional Kelvin–Helmholtz perturbation analysis presented by Hewitt and Hall-Taylor (1970), such that the normal stress exerted by the gas core phase on the interface in an infinite gas medium can be expressed as:

$$N_{iG} = \overline{N}_{iG} - k\hat{m}\rho_{gc}(\bar{u}_{gc} - c)^2 e^{ikz} \tag{4}$$

3.1.2. Liquid film analysis

A similar perturbation analysis was used to arrive at an expression for the normal stress at the interface due to the liquid film (Holowach, 2002). But, in this particular case, a shallow film correction was employed in this derivation, deviating from the assumptions of Hewitt and Hall-Taylor (1970). Employing the shallow film correction for the wavelength determination results in ~20–30% difference in the wavelength calculation as compared to the case where the correction is not used for typical steam–water annular flows.

Similar to the end result of the gas core stability analysis, an expression was arrived at for the normal stress exerted by the liquid phase on the interface in terms of the film thickness, liquid density, film velocity, wave number, and wave velocity:

$$N_{il} = \overline{N}_{il} + \rho_l \hat{m}(\bar{u}_l - c)^2 \frac{\cosh[k\bar{m}] - 1}{\sinh[k\bar{m}]} e^{ikz} \tag{5}$$

For cases where the wavelength is considerably greater than the film thickness, Eq. (5) could be further simplified by eliminating the hyperbolic terms. In Hewitt and Hall-Taylor's (1970) interfacial stability calculation, these terms are eliminated. But, this is contrary to the observations of Woodmansee and Hanratty (1969) and Cohen and Hanratty (1965), where it appears that the primary means of droplet entrainment in annular two-phase flow is driven by waves that have a wavelength on the order of magnitude of the film thickness. Therefore, when considering the short wavelengths that are characteristic of the observations in annular film flow entrainment, the hyperbolic terms cannot be neglected.

3.1.3. Analysis of the combined effects of the gas core and the liquid film

The stability conditions for inviscid annular two-phase flow can now be found by relating the normal stresses across the interface. A diagram of the normal stresses at the interface, and the requisite coordinate systems used to conduct the separate liquid film and gas core analyses is given in Fig. 5. Accounting for the different coordinate systems ($r = 0$ at the gas core centerline for the gas core analysis, and $y = 0$ at the wall for

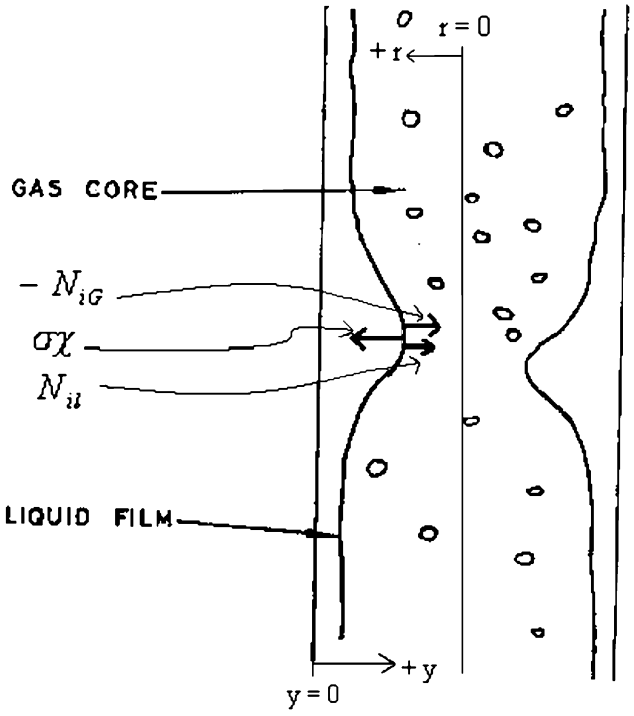

Fig. 5. Stresses and coordinate systems for the interfacial stability calculation.

the liquid film analysis), a balance of the gas normal stress, liquid normal stress, and surface tension force is given as:

$$N_{il} - N_{ig} = \sigma\chi \tag{6}$$

where χ is the curvature of the interface that is expressed as:

$$\chi = k^2 \hat{m} e^{ikz} \tag{7}$$

By substituting Eqs. (4), (5) and (7) into Eq. (6); and by canceling the exponential and perturbed film thickness terms, combining the wave number terms, and canceling the average normal stress exerted by the gas and liquid phases at the interface, the following characteristic equation for wave motion is arrived at:

$$\rho_l(\bar{u}_l - c)^2 \frac{\cosh[k\bar{m}] - 1}{\sinh[k\bar{m}]} + \rho_{gc}(\bar{u}_{gc} - c)^2 = \sigma k \tag{8}$$

It must be noted that Eq. (8) is valid for the physical constraint for upward, co-current annular flow where $\bar{u}_{gc} > \bar{u}_l$. The quadratic equation, above, can be solved for the real and imaginary parts of the wave velocity as given by:

$$c_R = \frac{((\cosh[k\bar{m}] - 1)/\sinh[k\bar{m}])\rho_l\bar{u}_l + \rho_{gc}\bar{u}_{gc}}{((\cosh[k\bar{m}] - 1)/\sinh[k\bar{m}])\rho_l + \rho_{gc}} \tag{9}$$

$$c_I = \pm\left[-\frac{\cosh[k\bar{m}] - 1}{\sinh[k\bar{m}]}\rho_l\rho_{gc}(\bar{u}_{gc} - \bar{u}_l)^2 + \sigma k\left(\frac{\cosh[k\bar{m}] - 1}{\sinh[k\bar{m}]}\rho_l + \rho_{gc}\right)\right]^{1/2} \times \left(\frac{\cosh[k\bar{m}] - 1}{\sinh[k\bar{m}]}\rho_l + \rho_{gc}\right)^{-1} \tag{10}$$

Assuming no imaginary components to the wave velocity for a stable wave, the critical wavelength, λ_c, for the condition of neutral stability ($c_I = 0$), is subsequently solved for by setting the numerator of the above equation to zero. Substituting the wave number, k, which is equal to $k = 2\pi/\lambda_c$ into the numerator of the imaginary wave velocity, a stability condition is arrived at that can be solved iteratively for the critical wavelength:

$$-\frac{\left(\cosh\left[\frac{2\pi}{\lambda_c}\bar{m}\right] - 1\right)}{\sinh\left[\frac{2\pi}{\lambda_c}\bar{m}\right]}\rho_l\rho_{gc}(\bar{u}_{gc} - \bar{u}_l)^2 + \sigma\frac{2\pi}{\lambda_c}\left(\frac{\cosh\left[\frac{2\pi}{\lambda_c}\bar{m}\right] - 1}{\sinh\left[\frac{2\pi}{\lambda_c}\bar{m}\right]}\rho_l + \rho_{gc}\right) = 0 \tag{11}$$

The critical wavelength is not readily solved for explicitly since it appears in several terms in the above equation, but can be solved for utilizing a numerical method. With the critical wavelength, the wave number (k) can be calculated to determine the real wave velocity, C_R, from Eq. (9), which was developed in the perturbation analysis.

3.2. Wave crest force balance

Utilizing the methodology of an inviscid pressure stress analysis, developed in the previous section from that of Hewitt and Hall-Taylor (1970), normal to the axis of the flow, a critical wavelength can be calculated when the wave becomes unstable for a given set of fluid conditions. With this critical wavelength, a wave geometry can subsequently be characterized for a force balance on the wave crest, along the axis of the flow. The force balance on a wave crest must also consider viscous effects in order to perform the detailed analysis needed to determine the maximum volume of liquid that can be entrained.

A three-dimensional sine wave geometry is assumed as it provides a more simplified means of quantification, and allows for flexibility for future model enhancement and analysis. In reality, the wave geometry differs from that of the sine wave by having a more truncated geometry on one end, but the sine wave is a reasonable estimate for the force balance and entrainment model development since as the wave crest and a droplet forms, the specific geometrical region approaches that of a sine wave more than something like a ring wave. The sine wave geometry is consistent with the interfacial instability calculation presented in the previous section. A three-dimensional sketch of the wave geometry to be considered for this analysis is presented in Fig. 6.

Previous modeling efforts by Ishii and Grolmes (1975) have also employed a force balance on a wave crest to determine the criteria for the inception of droplet entrainment. The wave crest force balance technique has also been used by Kataoka et al. (1983) to develop a correlation for the droplet size distribution in co-current

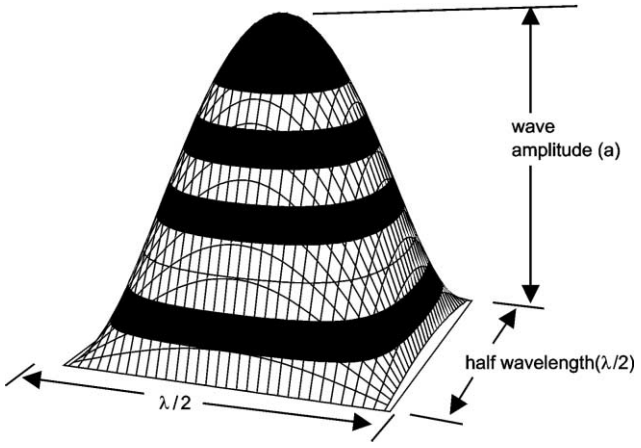

Fig. 6. Three-dimensional sine wave for co-current annular film flow entrainment modeling.

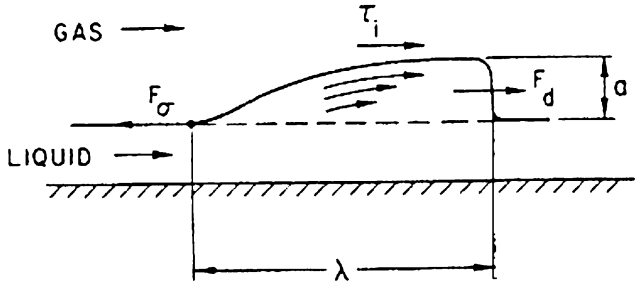

Fig. 7. Model for entrainment based on roll wave breakup used by Ishii and Grolmes (1975) and Kataoka et al. (1983).

annular two-phase flow. An illustration of the force balance technique along the axis of the flow on a distorted wave crest used by both Ishii and Grolmes (1975) and Kataoka et al. (1983), is given in Fig. 7. As can be seen in the figure, previous analyses have considered the drag force imparted by the gas flow, and the surface tension force that resists the deformation as part of the development of droplet entrainment models. The drag force, or interfacial shear, on the wave is due to the gas velocity being greater than the liquid film velocity in co-current annular flow. Since this analysis is specific to vertical upward co-current annular flow, a slightly different approach is taken in performing the force balance along the axis of flow to consider the interfacial drag force and surface tension force as well as the gravitational force on the wave crest. An illustration of the force balance on the wave crest used in this study is given below in Fig. 8.

This study also considers the effects of the gas core that is assumed to be composed of both vapor and droplets. The effect of the vapor and droplets results in a larger effective gas core density that impacts the drag force on the wave crest due to entrained droplet collisions into the wave crest. Nigmatulin et al. (1996) suggested that droplet de-entrainment has a resultant effect on droplet entrainment by momentum transfer to the film. The effect of having momentum induced by droplet collisions is partially accounted for by the use of an equivalent gas core density to calculate the drag force on

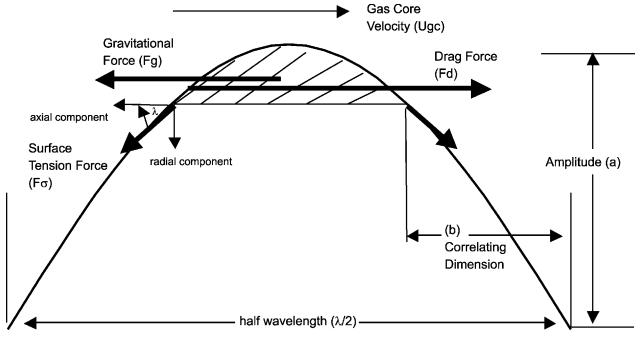

Fig. 8. Three-dimensional sine wave crest force balance for upward co-current annular two-phase flow representing the forces on a ripple.

the wave crest. The drag force is also calculated by the assumption of an area-based drag coefficient, and the subsequent calculation of the effective area normal to the flow that the wave crest presents. The gravitational force on the wave crest is calculated by an estimation of the volume of the wave crest. The primary effects of the surface tension force are postulated to occur when the wave crest begins to deform prior to droplet breakup from the crest, since, for a symmetric wave the surface tension force on the wave crest cancels in the axial direction. As the wave begins to deform, the surface tension force along the axis of the flow becomes greater since a radius of curvature and the area over which the surface tension force acts increases along the back side of the wave.

A key assumption in the development of this droplet entrainment model is that the maximum amount of liquid that can be entrained from a wave crest occurs when the vector sum of these force components equals zero. This situation does not directly consider droplet inertia effects, but simply calculates the maximum possible volume of liquid that can be entrained from a wave. The force balance on the wave crest along the axis of the flow is given by:

$$\vec{F}_{\mathrm{d}} + \vec{F}_{\mathrm{g}} + \vec{F}_{\sigma} = 0 \tag{12}$$

By solving the force balance given in Eq. (12), a determination of the maximum amount of liquid that can be entrained from a wave crest can be calculated for a given set of fluid conditions, and can be compared to experimental data so as to arrive at an expression for the average liquid droplet entrainment rate.

3.2.1. Wave crest drag force calculation

In performing a force balance on the wave crest, it is necessary to calculate the effective area on which the drag force imposes. The drag force is calculated by selecting a drag coefficient, and using the relative velocity between the wave crest and the gas core, along with the average of the gas core and vapor densities to arrive at an equivalent boundary layer density ($\rho_{\mathrm{g,bl}}$). The use of a boundary layer density for the mixture impacting the wave crest departs from the inviscid gas flow approximation and results in a more realistic estimation of the drag force on the wave crest. The use of a mixture density is substantiated by the measurements of Gill et al. (1964) that show the variation in the local liquid distribution across a tube in fully developed annular film flow. The drag force is given as:

$$F_{\mathrm{d}} = \frac{1}{2}\rho_{\mathrm{g,bl}} C_{\mathrm{D}} A_{\mathrm{entr,w}} (\bar{u}_{\mathrm{g}} - c_{\mathrm{R}})^2 \tag{13}$$

Several assumptions must be made in order to perform the calculation of the drag force on a wave crest. First, a drag coefficient (C_{D}) must be estimated for a given wave geometry. A drag coefficient (based on frontal area) has

been estimated using the results of the droplet size and interfacial area analysis of Kataoka et al. (1983). The mean gas velocity and mean liquid film velocities can be calculated using the void fraction and liquid film predictions from a thermal hydraulic computer code, such as COBRA-TF. The area on which the drag force acts is more difficult to evaluate, but can be calculated by assuming that the wave takes a sinusoidal shape. The sinusoidal shape is assumed to be a three-dimensional body (Fig. 6). The wave crest is assumed to be moving in the axial direction at the real wave velocity given by Eq. (3).

In their analysis, Kataoka et al. (1983) calculated a Weber number for the volume median diameter of a droplet based on the results of a range of experimental data. They also related the drag coefficient on the wave crest to the Weber number. In using their correlation of various sets of experimental data, the drag coefficient for the wave crest can be expressed in terms of the film Reynolds number (Re_f), gas Reynolds number (Re_g), and the gas and liquid densities (ρ) and viscosities (μ) as:

$$C_D = 286 Re_f^{1/6} Re_g^{-2/3} \left(\frac{\rho_g}{\rho_f}\right)^{1/3} \left(\frac{\mu_g}{\mu_f}\right)^{-2/3} \tag{14}$$

A view of the sine wave that is used to model the ripples observed in annular flow is shown in Fig. 9. The parameter, a, is the amplitude of the sine wave, $\tilde{a}$ is the height of the wave crest that is sheared off, and λ_c is the critical wavelength calculated in Eq. (10). The sine wave for this model is assumed to be at the critical wavelength, and b is the distance from the y-axis to the point of the sine wave at height $a - \tilde{a}$. This parameter will be used to relate the various components of the force balance on the wave crest, and is solved by an iterative solution.

An equation for the sine wave pictured in Fig. 9, is given in terms of the amplitude (a) and the wavelength (λ), by:

$$y = a \sin\left(\frac{2\pi x}{\lambda}\right) \tag{15}$$

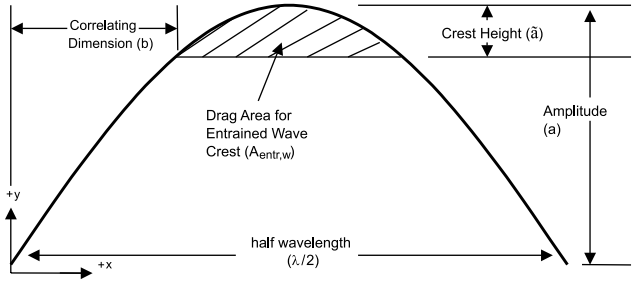

Fig. 9. View facing the three-dimensional sine wave detailing the drag area on the ripple wave crest.

Therefore, the effective drag area which is normal to the flow ($A_{entr,w}$) is expressed in terms of the integral of Eq. (15):

$$A_{entr,w} = \int_b^{\lambda/2-b} a \sin\left(\frac{2\pi x}{\lambda}\right) dx - [a - \tilde{a}]\left(\frac{\lambda}{2} - 2b\right) \tag{16}$$

The height ($a - \tilde{a}$) can be expressed in terms of the geometric correlating parameter "b" (used to characterize the ripple geometry) and the wavelength:

$$[a - \tilde{a}] = \sin\left(\frac{2\pi b}{\lambda}\right) \tag{17}$$

By performing the integration in Eq. (16), evaluating limits, and substituting the expression in Eq. (17), an expression for the effective drag area is arrived at:

$$A_{entr,w} = \frac{a\lambda}{2\pi}\left[\cos\left(\frac{2\pi b}{\lambda}\right) - \cos\left(\frac{2\pi\{\lambda/2 - b\}}{\lambda}\right)\right] - a \sin\left(\frac{2\pi b}{\lambda}\right)\left[\frac{\lambda}{2} - 2b\right] \tag{18}$$

The wave amplitude "a" is determined using the modeling methodology employed by Ishii and Grolmes (1975) which assumes that the motion of the wave crest with respect to the liquid film can be expressed by a shear flow model where the amplitude is quantified in terms of the shear stress (τ_i), the film velocity (v_f), and a dimensionless parameter (C_w) which accounts for the effect of the surface tension on the internal flow:

$$a = C_w \mu_f \frac{v_f}{\tau_i} \tag{19}$$

As an approximation to the case of wave formation in vertical annular flow, gravitational forces are neglected since this analysis calculates the wave height, a, in the radial direction (Ishii and Grolmes, 1975). For horizontal flow analysis, gravitational effects on the wave crest height are expected to be much greater. Since the hydrodynamics inside of the wave crest can be described in terms of the viscous and surface forces, C_w is a function of these forces (Ishii and Grolmes, 1975). Therefore, C_w will be assumed to be a function of the viscosity number, N_μ:

$$C_w = C_w(N_\mu) \tag{20}$$

The viscosity number, N_μ, was developed based on the length scale of a Taylor instability analysis which gives the maximum stable drop radius in a free stream. Sleicher (1972) showed that the viscosity number group measures the viscous force induced by an internal flow to the surface tension force based on the internal flow induced by a natural vibration of a drop. Also, the inverse square of the viscosity number is known as the Archimedes number that has been used to correlate experimental data in the slug and bubbly flow regimes. The viscosity number is given as:

$$N_\mu = \frac{\mu_f}{\left(\rho_f \sigma \left\{\frac{\sigma}{g\Delta\rho}\right\}^{1/2}\right)} \tag{21}$$

The experimental value of C_w was correlated in terms of the viscosity number by Ishii and Grolmes (1975) using a variety of experimental data covering a range of geometries, fluids, and flow conditions. The curve fit given by Ishii and Grolmes (1975) for determining the value of C_w is given in the following relation:

$$\begin{aligned} \frac{1}{3C_w} &= 11.78 N_\mu^{0.8} \quad \text{for } N_\mu \leqslant \frac{1}{15} \\ \frac{1}{3C_w} &= 1.35 \quad \text{for } N_\mu > \frac{1}{15} \end{aligned} \tag{22}$$

The shear force at the interface can be modeled by either using a gas or liquid friction factor. In order to provide closure on the calculation of the wave amplitude using the shear flow model of Ishii and Grolmes (1975) given in Eq. (19), the shear stress at the interface can be expressed in terms of the liquid interfacial friction factor (f_{il}) as:

$$\tau_i = f_{il} \frac{\rho_f v_f^2}{2} \tag{23}$$

In solving for the amplitude in Eq. (19), the film velocity term can be eliminated by the substitution of Eq. (23), resulting in an expression for wave amplitude that is dependent on fluid properties and interfacial shear as:

$$a = \frac{\sqrt{2} C_w \mu_f}{(\rho_f \tau_i f_{il})^{1/2}} \tag{24}$$

An expression for the interfacial liquid film friction factor has been developed by Ishii and Grolmes (1975) for $Re_f > 1000$, and is based on the film thickness given by the work of Hughmark (1973):

$$(f_{il})^{1/2} = 0.735 Re_f^{-0.19} \tag{25}$$

Eq. (25) is substituted into Eq. (24) to eliminate the interfacial friction factor term:

$$a = \frac{\sqrt{2} C_w \mu_f}{\{\rho_f \tau_i\}^{1/2} (0.735 Re_f^{-0.19})} \tag{26}$$

In order to complete the calculation of the drag force on a wave crest, it is necessary to calculate the interfacial shear to solve Eq. (26). The correlation of Whalley and Hewitt (1978) has been selected for the calculation of the interfacial shear, since it was developed based on a variety of gases and liquids over a range of conditions including steam–water. The interfacial shear stress is expressed as:

$$\tau_i = \frac{f_{ig} \rho_{gc} V_{gc,sup}^2}{2} \tag{27}$$

The film interfacial film friction factor (f_{ig}) is based on the superficial gas core mixture velocity ($V_{gc,sup}$) which is given in terms of the vapor and entrained mass fluxes (G_g and G_e, respectively):

$$V_{gc,sup} = \frac{G_g}{\rho_g} + \frac{G_e}{\rho_f} \tag{28}$$

The interfacial friction factor (f_{ig}) is correlated in terms of the film thickness (m), the hydraulic diameter (D_H), the liquid and vapor densities, and the gas core Reynolds number (Re_{gc}) as:

$$f_{ig} = 0.079 Re_{gc}^{-1/4} \left[1 + 24 \left(\frac{\rho_f}{\rho_g}\right)^{1/3} \frac{m}{D_H}\right] \tag{29}$$

The gas core Reynolds number used for this correlation is defined as:

$$Re_{gc} = \frac{(G_g + G_e) D_H}{\mu_g} \tag{30}$$

From the interfacial shear term, which is subsequently used to calculate the wave amplitude "a", it can be seen that overall system parameters such as superficial core mixture velocity are used to calculate a very local interfacial shear effect. An assumption of average effects on the interface must be made to use mean flow rates. Furthermore, most interfacial drag correlations, such as the one used in this analysis, are based on larger-scale parameters (i.e. flow rates, densities, viscosities) that can be readily measured in an experimental environment. Therefore, in an attempt to make this analysis plausible, such extensions from a very local phenomenon to a system parameter must be made, and the verification that such assumptions are valid can be assessed by trend analysis evaluation of the proposed model with experimental data.

3.2.2. Wave crest gravitational force calculation

As part of the axial force balance on a wave crest in vertical annular flow, it is necessary to calculate the volume of the wave crest in order to account for the gravitational force on the wave crest. The final form of the expression for the volume of the wave crest should be in terms of the correlating dimension, b, shown in Fig. 9, such that an iterative solution of the force balance may be conveniently obtained.

It is convenient to assume the following form of the wave equation thereby allowing for a volume integration to be performed about the y-axis, using the disc method:

$$y = a \cos\left(\frac{2\pi x}{\lambda}\right) \tag{31}$$

By utilizing the disc integration method over the limits depicted in Fig. 9 and by substituting Eq. (17), the following expression for the wave crest volume is given in terms of the correlating parameter "b":

$$V_{\mathrm{entr,w}} = \frac{a\lambda^2}{4\pi}\left[-2 + 2\sin\left(\frac{2\pi b}{\lambda}\right) + 2\left\{1 - \sin^2\left(\frac{2\pi b}{\lambda}\right)\right\}^{1/2} \arccos\left\{\sin\left(\frac{2\pi b}{\lambda}\right)\right\} - \sin\left(\frac{2\pi b}{\lambda}\right)\left\{\arccos\left(\sin\left\{\frac{2\pi b}{\lambda}\right\}\right)\right\}^2\right] \tag{32}$$

Using the calculated volume of the wave crest, the gravitational force on the crest is calculated for upward vertical flow, with the upward direction being defined as the positive direction:

$$\vec{F}_{\mathrm{g}} = -\rho_{\mathrm{f}} V_{\mathrm{entr,w}} g \tag{33}$$

3.2.3. Wave crest surface tension force calculation

To calculate the surface tension force that acts to maintain the wave crest geometry, and thereby resists the entrainment of the wave crest, several assumptions must be made to estimate the curvature and the effective area such that the surface tension force component can be evaluated. Since the wave crest easily deforms, some simplifying geometrical assumptions are made:

1. The average curvature of the wave crest can be estimated as the curvature at the peak of a sine wave of amplitude "a" and wavelength "λ" as depicted in Fig. 10.
2. The area on which the surface tension force acts can be calculated by assuming a circle with one-half the diameter of the dimension ($\lambda/2 - 2b$) as depicted in Figs. 8 and 10. The reasoning behind this assumption is that as a wave deforms, the crest will be "stretched," thereby making the area in which it maintains contact with the rest of the wave to decrease. As a first approximation, it is assumed that the radius of contact with the wave decreases by a factor of two as the wave crest is stretched.

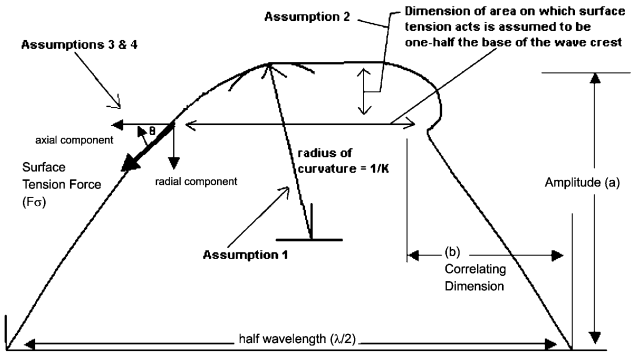

Fig. 10. Assumptions of the geometry of the deforming wave for the surface tension force calculation.

3. The surface tension force vector acts along the slope of the sine wave depicted in Fig. 10, so as to resist deformation of the wave crest. The component of the force along the axis of the flow can be determined using geometrical relations, and the derivative (slope) of the sine function can be evaluated at a given point. The point that is used in the estimation of the slope is assumed to be that characterized by the base of the wave crest as depicted in Fig. 10.
4. The surface tension force acts on the front of the wave only, since as the wave crest deforms, the rear of the wave flattens, resulting in a minimal surface tension force along the axial direction of the flow.

Assuming that the wave geometry can be approximated by the sketch in Fig. 10, and quantified by Eq. (15), the curvature, K, for an arbitrary point on the wave is calculated by operating on Eq. (15):

$$K = \frac{\left| -\frac{4\pi^2 a}{\lambda^2}\sin\left(\frac{2\pi x}{\lambda}\right)\right|}{\left(1 + \left[\frac{2\pi}{\lambda}\cos\left(\frac{2\pi x}{\lambda}\right)\right]^2\right)^{3/2}} \tag{34}$$

Since it is assumed for this analysis that the average curvature of the wave crest ($K_{\mathrm{crest,avg}}$) is expressed by the curvature at the peak of the sine wave (see Assumption #1), Eq. (34) is evaluated at $x = \lambda/4$ for use in the surface tension force calculation:

$$K_{\mathrm{crest,avg}} = \frac{4\pi^2 a}{\lambda^2} \tag{35}$$

Using Assumption #2 which states that the effective area on which the surface tension acts is equal to the area given by one-half the radius considered where $x = b$ on the sine wave depicted in Figs. 9 and 10, the area "A_σ" on which the surface tension force acts on is given by:

$$A_\sigma = \pi\left(\frac{\lambda/4 - b}{2}\right)^2 \tag{36}$$

Using the relations arrived at for the area on which the surface tension acts and the curvature, the surface tension force vector is expressed as:

$$\vec{F}_\sigma = \sigma K_{\mathrm{crest,avg}} A_\sigma \tag{37}$$

The slope of the sine wave pictured in Figs. 9 and 10 is determined by differentiating Eq. (15):

$$\frac{\mathrm{d}y}{\mathrm{d}x} = \frac{2\pi a}{\lambda}\cos\left(\frac{2\pi x}{\lambda}\right) \tag{38}$$

Since the slope of the sine wave is equal to the tangent of angle θ, the value of θ at $x = b$ is given as:

$$\theta = \arctan\left[\frac{2\pi a}{\lambda}\cos\left(\frac{2\pi b}{\lambda}\right)\right] \tag{39}$$

The component of the surface tension force that acts on the front of the wave crest, along the axis of the flow can be expressed as:

$$F_{\sigma,\text{axis}} = -\vec{F}_{\sigma}\cos(\theta) \tag{40}$$

Substituting Eqs. (35)–(37) and (39) into Eq. (40), gives a simplified expression for the estimate of the surface tension force that acts on the wave crest along the axial direction:

$$F_{\sigma,\text{axis}} = -\frac{4\pi^3 a\sigma}{\lambda^2}\left(\frac{\lambda/4-b}{2}\right)^2 \times \cos\left(\arctan\left[\frac{2\pi a}{\lambda}\cos\left(\frac{2\pi b}{\lambda}\right)\right]\right) \tag{41}$$

3.2.4. Combined wave crest force balance

The combined force balance on the wave crest for the maximum volume of entrained liquid is arrived at by summing the effects of the drag, gravity, and surface tension forces. Eqs. (13), (14), (18), (32), (33) and (41) are substituted into Eq. (12) to arrive at the final expression for the wave crest force balance:

$$\begin{aligned}&\frac{1}{2}\rho_{\text{g,bl}}C_{\text{D}}\left\{\frac{a\lambda}{2\pi}\left[\cos\left(\frac{2\pi b}{\lambda}\right)-\cos\left(\frac{2\pi\{\lambda/2-b\}}{\lambda}\right)\right]\right.\\&\left.-a\sin\left(\frac{2\pi b}{\lambda}\right)\left[\frac{\lambda}{2}-2b\right]\right\}(\bar{u}_{\text{g}}-c_{\text{R}})^2-\rho_{\text{f}}g\frac{a\lambda^2}{4\pi}\\&\times\left[-2+2\sin\left(\frac{2\pi b}{\lambda}\right)+2\left\{1-\sin^2\left(\frac{2\pi b}{\lambda}\right)\right\}^{1/2}\right.\\&\times\arccos\left\{\sin\left(\frac{2\pi b}{\lambda}\right)\right\}-\sin\left(\frac{2\pi b}{\lambda}\right)\\&\left.\times\left\{\arccos\left(\sin\left\{\frac{2\pi b}{\lambda}\right\}\right)\right\}^2\right]-\frac{4\pi^3 a\sigma}{\lambda^2}\left(\frac{\lambda/4-b}{2}\right)^2\\&\times\cos\left(\arctan\left[\frac{2\pi a}{\lambda}\cos\left(\frac{2\pi b}{\lambda}\right)\right]\right)=0\end{aligned} \tag{42}$$

Eq. (42) can subsequently be iteratively solved for the correlating dimension "b". The value of b is then substituted into Eq. (32) in order to determine the maximum volume of liquid that can be entrained from a wave ($V_{\text{entr,w}}$). Knowing $V_{\text{entr,w}}$ and the wavelength λ, the rest of the parameters in Eq. (1) may be solved for in order to calculate the droplet entrainment rate. To facilitate the determination of the droplet entrainment rate, a control volume of height λ, depicted in Fig. 2, is assumed. Note that in utilizing this proposed force balance method, as the film thickness approaches zero, both the drag coefficient given in Eq. (14) and the wave amplitude in Eq. (26) approach zero, yielding a decreased entrained droplet volume as the film becomes "very thin".

The interfacial area of the control volume "A_{cv}" is given in terms of the continuous liquid volume fraction α_{l}, the wavelength, and the wetted perimeter "P_{w}" as:

$$A_{\text{cv}} = P_{\text{w}}\lambda(1-\alpha_{\text{l}})^{1/2} \tag{43}$$

The period of the entrainment phenomena in the control volume $\tau_{\text{w,cv}}$, which is related to the time scale by which droplets are swept off the film surface, is estimated from the time scale that the gas core passes over the liquid film:

$$\tau_{\text{w,cv}} = \frac{\lambda}{\bar{u}_{\text{gc}}-\bar{u}_{\text{f}}} \tag{44}$$

The number of waves on the interfacial area of the control volume $N_{\text{w,cv}}$ is estimated as:

$$N_{\text{w,cv}} = \frac{P_{\text{w}}}{\lambda} \tag{45}$$

Substituting Eqs. (43)–(45) an expression for the entrainment rate is arrived at:

$$S_{\text{E}} = \frac{V_{\text{entr,w}}\rho_{\text{f}}(\bar{u}_{\text{gc}}-\bar{u}_{\text{f}})}{\lambda^3\{1-\alpha_{\text{l}}\}^{1/2}} \tag{46}$$

Eq. (46) can be considered an estimate of the maximum possible entrainment mass flux in upward co-current annular flow. The next step in the model development is to compare the predictions of Eq. (46) to a set of experimental data, so as to determine a means for modifying Eq. (46) to predict an average, vice maximum, entrainment mass flux.

4. Development of an expression for the average entrainment rate

In order to determine the average droplet entrainment rate, a comparison of the predictions of Eq. (46) with that of the experimental data of Hewitt and Pulling (1969) and Keeys et al. (1970) has been conducted. The prediction of Eq. (46) reflects the *maximum* possible droplet entrainment rate based on the "zero" force balance assumption delineated in Section 3.2 (Eq. (12)), therefore it must be corrected to calculated the *average* droplet entrainment rate. The 42 data points that were selected for this portion of the model development were taken at various fluid conditions covering a range of pressures 0.239 MPa (34.7 psia) to 6.90 MPa (1000 psia).

Since such parameters have generally not been measured in fundamental steam–water entrainment tests, the COBRA-TF thermal hydraulic code (Thurgood et al., 1983) was utilized to estimate such conditions as film thickness, film velocity, entrained flow rate, droplet entrainment rate, and void fraction. Since these results were anticipated to possibly be in error due to deficiencies in the entrainment and drag models, the code output was then corrected, utilizing a spreadsheet, to

better-reflect the subchannel parameters corresponding to the experimentally measured entrained mass flow rate by means of a ratio of code-predicted to experimentally measured entrained mass flow rate. One must note that inherent errors within the various code models could become lumped into the results of these analyses, but, since such detailed subchannel data are not readily available, a forthright attempt was made to estimate these parameters. For example, an error in the code de-entrainment model which was developed by Thurgood et al. (1983) and based on the findings of Whalley (1977) could be reflected in the reduced subchannel data obtained from the computer code. The test of the validity of this recursive method of data reduction for model development is conducted in Section 5 by comparing the results of the corrected model to independent sets of experimental data over a wider range of conditions than those used in the model development.

With the corrected calculational subchannel data, a Microsoft Excel Spreadsheet was then used to solve for the maximum postulated entrainment rate (Eq. (46)) for the cases examined. The calculated maximum droplet entrainment rate (mass flux) for the Hewitt and Pulling (1969) and Keeys et al. (1970) experimental data are presented in Fig. 11. The results are presented as a ratio of the corrected experimental entrainment rate divided by the droplet entrainment rate predicted by this physical model, plotted as a function of the film Reynolds number.

The results of the model predictions plotted in Fig. 11 fall around the value of 0.005 for a large portion of the data which is consistent with the experimental analysis of Kataoka et al. (1983) which showed that the ratio of mean droplet volume to the maximum droplet volume is approximately equal to 0.0043. Assuming that the droplet entrainment rate is related to the maximum and average sizes of entrained droplets, this "order of magnitude" evaluation confirms the underlying combination of time scales and length scales in the proposed model when the ratio of *average* experimental entrainment rate to the *maximum* possible entrainment rate (Eq. (46)) are compared. An explanation for the data "tailing off" at

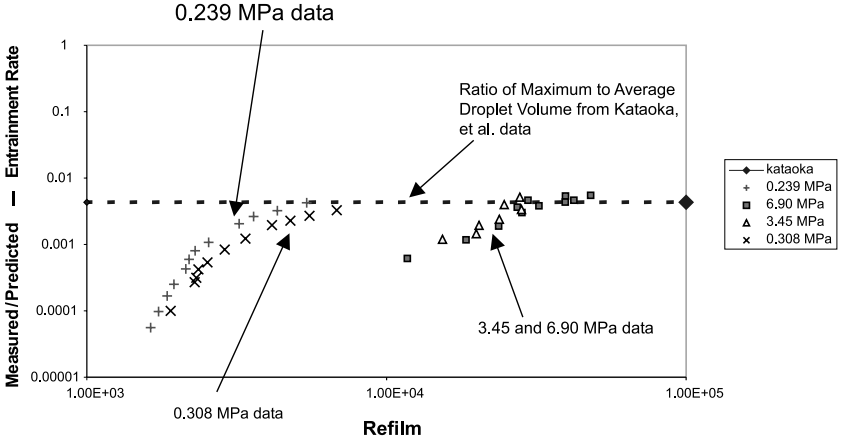

Fig. 11. Experimental/model predicted entrainment rate versus film Reynolds number for the Hewitt and Pulling (1969) 0.239 and 0.308 MPa (34.7 and 44.7 psia) data and the Keeys et al. (1970) 3.45 and 6.90 MPa (500 and 1000 psia) data.

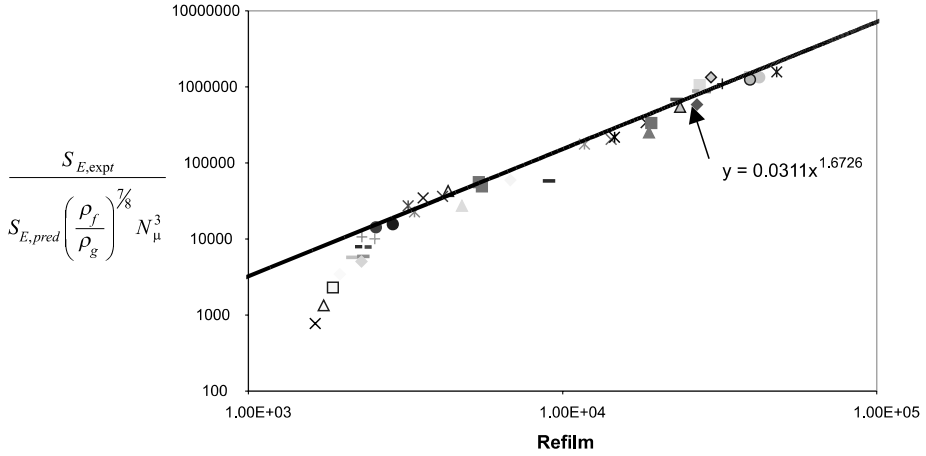

Fig. 12. Pressure-corrected plot of experimental/model predicted entrainment rate versus film Reynolds number.

film Reynolds numbers less than 3000 is that the shear flow model used for determining the wave amplitude is based on turbulent flow. It also appears from the plot of the data in Fig. 11 that there are some pressure effects not fully taken into account in the submodels employed in this analysis.

By introducing a pressure correction factor, and re-plotting the data as a function of film Reynolds number, a usable correlation is obtained as given in Fig. 12. The means of correction of pressure effects that are used in this analysis are the ratio of the fluid density to the vapor density, and the viscosity number given by Eq. (13). The empirical density ratio and viscosity number corrections to the correlation account for pressure-related phenomena that have an impact on the interfacial drag and viscosity effects, while the Reynolds number correction accounts for the use of an inviscid stability analysis as well as other related closure model deficiencies.

The pressure-corrected form of Eq. (46) for calculating the entrainment rate can now be given as:

$$S_{\mathrm{E}} = 0.0311 Re_{\mathrm{film}}^{1.67} \left(\frac{\rho_{\mathrm{f}}}{\rho_{\mathrm{g}}}\right)^{7/8} N_{\mu}^{3} \frac{V_{\mathrm{entr,w}} \rho_{\mathrm{f}} (\bar{u}_{\mathrm{gc}} - \bar{u}_{\mathrm{f}})}{\lambda^{3} \{1 - \alpha_{\mathrm{l}}\}^{1/2}} \qquad (47)$$

A linear numerical transition can also be applied to account for flow transition effects at low film Reynolds numbers (<3000) that may not be modeled by the use of a turbulent shear model for the wave amplitude in the wave crest force balance calculation. Such a factor would serve as a multiplier on the entrainment model to "ramp" the predicted entrainment rate value from zero at a low Reynolds number limit (i.e. 1000), and up to 100% of the value predicted by Eq. (47) at a Reynolds number of 3000. This entrainment rate model given in Eq. (47) can subsequently be implemented into a two-phase systems analysis computer code, such as COBRA-TF, and then used for the calculation of the entrainment rate in co-current vertical annular flow.

5. Comparison of the proposed model with independent test data

The droplet entrainment rate model that has been developed was primarily based on a physical derivation, along with the use of 42 data points from the Hewitt and Pulling (1969) and Keeys et al. (1970) entrainment experiments. In order to provide an independent evaluation of the proposed physical model, the model

Table 1
Range of experimental conditions for the evaluation of the annular flow entrainment model

Data source	No. of data points	Pressure (MPa)	Film Reynolds number	Gas Reynolds number	Test section inner diameter (mm)	Test section length (m)	L/D
Hewitt and Pulling (1969)	51	0.239–0.446	1600–6800	46,000–150,000	9.30	1.83, 3.66	197, 393
Keeys et al. (1970)	18	3.45–6.90	12,000–48,000	240,000–620,000	12.6	3.66	290
Singh (1967)	25	6.90–8.28	3800–42,000	110,000–450,000	12.5	~2.4	195
Wurtz (1978)	60	3.04–9.13	11,000–57,000	84,000–660,000	10.0	9.0	898

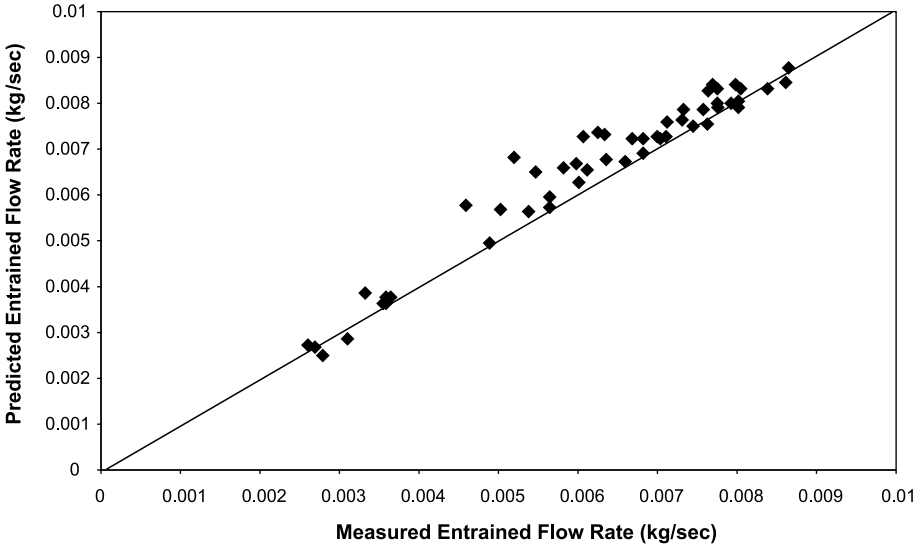

Fig. 13. Measured vs. predicted entrained flow rates for the Hewitt and Pulling data using the present annular flow entrainment model.

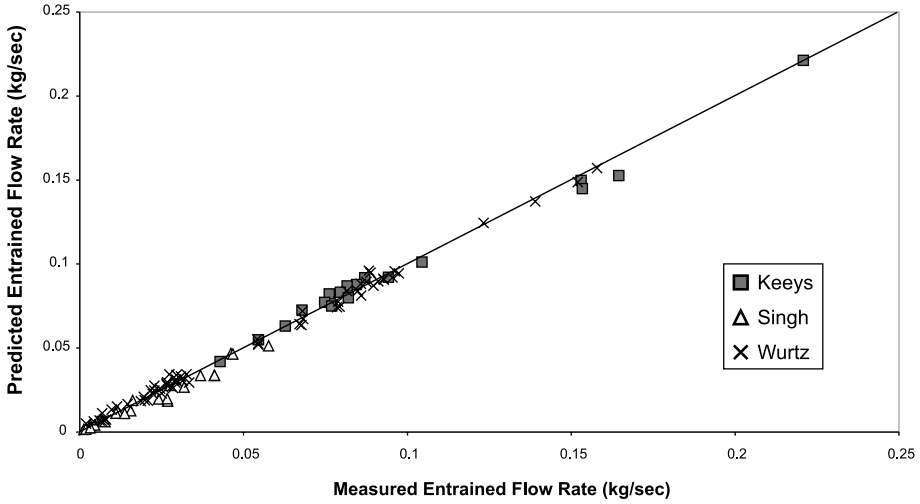

Fig. 14. Measured vs. predicted entrained flow rates for the Keeys et al., Singh, and Wurtz data using the present annular flow entrainment model.

predictions have been compared with independent experimental data. This evaluation of the model has been conducted utilizing the COBRA-TF thermal hydraulic systems analysis computer code upgraded with the proposed annular flow entrainment model. Annular flow entrainment data were selected based on having a superficial vapor velocity at least 50% above the critical superficial vapor velocity for droplet entrainment as given by Ishii and Grolmes (1975). This means of selecting data for comparison ensures an annular flow regime with dispersed droplet flow, and is consistent with the means in which Lopez de Bertodano et al. (1994) developed their correlation for the amount of entrained liquid. Code input models were constructed of the various test facilities, and each specific entrainment test that was modeled was run until a steady state existed, such that comparisons on the entrained mass flow rate exiting the test section, and test section pressure drop could be performed.

A summary of the range of conditions for the data for which the physical entrainment model was compared to is given in Table 1. All experimental data for comparison were chosen from steam–water tests since the primary intent for the use of this model is to predict entrainment in steam–water systems such as nuclear reactor cores. As can be seen in Table 1, an overlapping range of data is available. The data for comparison range in pressures from 0.239 to 9.13 MPa (34.7 to 1323 psia), film Reynolds numbers from 1600 to 57,000, gas Reynolds numbers from 46,000 to 660,000, test section diameters from 9.30 to 12.6 mm (0.366–0.497 in.), and L/D ratios varying from 195 to 898. This range of data used for comparison extends beyond the original data sets used for the model development, and provides a reasonable means of evaluation for the pressure-corrected film Reynolds number curve fit since the Singh (1967) data test the low film Reynolds number entrainment at high pressure, where the low film Reynolds number portion of the curve was based on the low pressure data from Hewitt and Pulling (1969). It also should be noted that in addition to entrainment/film flow data, the Singh (1967) and Wurtz (1978) data sets provide pressure drop data for comparison as well.

A plot of the measured versus predicted entrained flow rates for the Hewitt and Pulling data set is given in Fig. 13, while a plot of the measured versus predicted entrained mass flow rate for the Keeys et al., Singh, and Wurtz data sets is given in Fig. 14. It can readily be seen that over a large range of entrained mass flow rates, a satisfactory prediction of the entrained flow rate is made using the proposed model.

Table 2
Summary of the comparison of the calculational results of entrained mass flow rate exiting the test section with the experimental data

Data set	Average error (proposed model) (%)	Average error (original COBRA-TF model) (%)
Hewitt and Pulling (1969)	6.80	39.6
Keeys et al. (1970)	3.76	3.63
Singh (1967)	14.1	18.7
Wurtz (1978)	10.9	15.4

Table 3
Summary of the comparison of the calculational results of the test section pressure drop with experimental data

Data set	Average error (proposed model) (%)	Average error (original COBRA-TF model) (%)
Singh (1967)	35.8	176
Wurtz (1978)	23.7	134

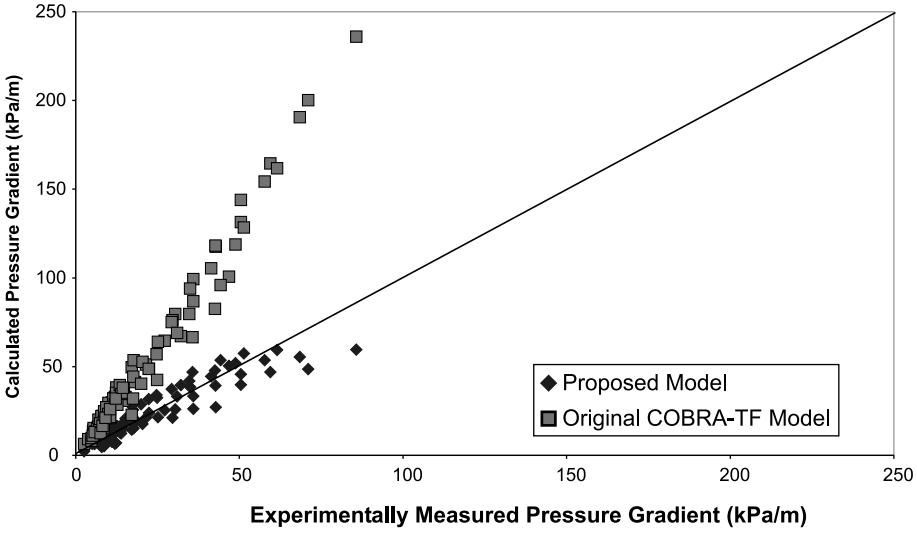

Fig. 15. Measured vs. predicted axial pressure gradients for the Singh and Wurtz data comparing the original COBRA-TF and present annular flow entrainment models.

The results of this analysis which are summarized in Table 2 indicate a significant improvement in the ability to predict annular film flow entrainment experimental data as compared to the predictions obtained from the original COBRA-TF annular entrainment model (Thurgood et al., 1983) which is based on an empirical polynomial fit to the Wurtz (1978) data.

Table 2 clearly demonstrates the significant improvement in the prediction of droplet entrainment in upward co-current annular flow using the proposed model as compared to the original annular film entrainment model (Thurgood et al., 1983) contained in the COBRA-TF thermal hydraulic systems analysis computer code. The average error for all of the data points was ~9% for the physical model proposed in this paper, while the original annular entrainment model had an average error of ~23% for all of the data points. From Table 2, it can be seen that that major improvement in the predictive capability of the droplet entrainment has been realized at the lower pressures, where the original COBRA-TF annular film droplet entrainment model performed poorly.

To further substantiate these findings, a comparison of the code predicted pressure drop is compared to the experimentally measured pressure drop data for the Singh (1967) and Wurtz (1978) experiments as given in Table 3. When viewing Table 3, one must note that the original COBRA-TF interfacial shear model (Thurgood et al., 1983) is based on air–water data (Wallis, 1969), and the interfacial shear model used for the proposed physical entrainment model is based on steam–water data (Whalley and Hewitt, 1978).

From Table 3 and Fig. 15, it is clearly seen that the entrainment and interfacial shear model proposed in the present study performs considerably better than the original COBRA-TF models, with roughly a factor of five reduction in the average and RMS errors. Since droplet entrainment in annular two-phase flow is strongly dependent on the interfacial shear (Hewitt and Hall-Taylor, 1970; Paik et al., 1985), it appears that the original COBRA-TF model was calculating the annular flow entrainment based on an incorrect value of the interfacial shear. The proposed physical model for entrainment also indicates a significant improvement in the pressure drop calculation that is indicative that the interfacial shear force has been more physically modeled.

6. Conclusions

An upward co-current annular flow entrainment model based on a stability analysis and a fundamental force balance has been developed in this paper and verified over a range of experimental entrainment and pressure drop data for steam–water flows. Key assumptions had to be made in order to develop this fundamental model, such as the wave crest force balance corresponding to a maximum possible entrained volume, and the extension of the inviscid flow stability calculation to turbulent situations. Though these assumptions are significant, verification against independent test data demonstrates that this proposed model satisfactorily predicts the entrainment rate over a wide range of conditions. From this analysis, it appears that a significant improvement in the capability of predicting annular flow entrainment and pressure drop can be achieved when a more physically based entrainment model is implemented in a thermal hydraulic systems analysis computer code such as COBRA-TF. The

success in the development of an improved model for such a complex phenomenon such as droplet entrainment in annular two-phase flow serves as a starting point for model refinement and the development of a physical model for droplet entrainment from a bubbling pool, froth region, or quench region as is characteristic of the quench front phenomenon observed and modeled in the water reactor reflood transient. The other key result for this model is that it was developed utilizing parameters that can be readily obtained from subchannel analysis, thereby making this model amenable to implementation into a transient two-phase fluid flow and heat transfer computer code.

References

Cohen, L., Hanratty, T., 1965. Generation of waves in the concurrent flow of air and a liquid. AIChE Journal 11, 138–144.

Gill et al., 1964. Sampling probe studies of the gas core in annular two-phase flow: II, studies of the effect of phase flow rates on phase and velocity distribution. Chemical Engineering Science 19, 665.

Hewitt, G., Hall-Taylor, N., 1970. Annular Two-Phase Flow. Pergamon Press, New York.

Hewitt, G., Pulling, D., 1969. Liquid Entrainment in Adiabatic Steam–Water Flow. AERE-R-5374, Harwell, England.

Holowach, M., 2002. A Physical model for predicting droplet entrainment in transient two-phase fluid flow and heat transfer systems analysis computer codes, Ph.D. Dissertation, Department of Mechanical and Nuclear Engineering, The Pennsylvania State University.

Hossfeld, L. et al., 1982. Interfacial Friction in Cocurrent Upward Annular Flow. EPRI NP-2326.

Hughmark, G., 1973. Film thickness, entrainment, and pressure drop in upward annular and dispersed flow. AIChE Journal 19, 1062.

Ishii, M., Grolmes, M., 1975. Inception criteria for droplet entrainment in two-phase concurrent film flow. AIChE Journal 21 (2).

Kataoka, I., Ishii, M., Mishima, K., 1983. Generation and size distribution of droplet in annular two-phase flow. Transactions of the ASME, Journal of Fluids Engineering 105 (June), 230–238.

Keeys, R., Ralph, J., Roberts, D., 1970. Liquid Entrainment in Adiabatic Steam–Water Flow at 500 and 1000 psia. AERE-R-6293, Harwell, England.

Lopez de Bertodano, M., Jan, C., Beus, S., 1994. Droplet Entrainment Correlation for High Pressure Annular Two-Phase Flow. WAPD-T-2071, Bettis Atomic Power Laboratory, West Mifflin, PA.

Lopez de Bertodano, M., Assad, A., Beus, S., 2001. Experiments for entrainment rate of droplets in the annular regime. International Journal of Multiphase Flow 27, 685–699.

Miesen, R., 1994. Hydrodynamic stability of liquid films. In: Proceedings of the IUTAM Symposium on Waves in Liquid/Gas and Liquid/Vapour Two-Phase Systems, Kyoto, Japan, May 1994.

Nigmatulin, R. et al., 1996. Entrainment and deposition rates in a dispersed-film flow. International Journal of Multiphase Flow 22 (1), 19–30.

Paik, C.Y., Hochreiter, L.E., Kelly, J.M., Kohrt, R.J. Analysis of FLECHT-SEASET 163 Rod Blocked Bundle Data Using COBRA-TF, NUREG/CR4166, WCAP 103 75, EPRI N-4111, October 1985.

Singh, K., 1967. Liquid film flow-rate measurement at elevated pressures, M.S. Thesis, University of Windsor, Windsor, Ontario, Canada.

Sleicher, C., 1972. Maximum stable droplet size in turbulent flow. AIChE Journal 8, 471.

Thurgood, M., et al., 1983. COBRA/TRAC A Thermal Hydraulic Code for Transient Analysis of Nuclear Reactor Vessels and Primary Coolant Systems, NUREG/CR-3046, US Nuclear Regulatory Commission.

Wallis, G., 1969. One-Dimensional Two-Phase Flow. McGraw-Hill, New York.

Whalley, P., 1977. The calculation of dryout in a rod bundle. International Journal of Multiphase Flow 13, 501–515.

Whalley, P., Hewitt, G., 1978. The Correlation of Liquid Entrainment Fraction and Entrainment Rate in Annular Two-Phase Flow, AERE-R-9187, Harwell, England.

Woodmansee, D., Hanratty, T., 1969. Mechanism for the removal of droplets from a liquid surface by a parallel air flow. Chemical Engineering Science 24, 299–307.

Wurtz, J., 1978. An Experimental and Theoretical Investigation of Annular Steam–Water Flow in Tubes and Annuli at 30 to 90 bar. RISO REPORT NO. 372, RISO National Laboratory, Roskilde, Denmark.

Zuber, N., et al., 1961. The hydrodynamic crisis in pool boiling of saturated and subcooled liquids, Part II, paper no. 27, International Heat Transfer Conference, Boulder, CO.